ACS Energy LETTERS

http://pubs.acs.org/journal/aelccp

Unassisted Highly Selective Gas-Phase CO_2 Reduction with a Plasmonic Au/p-GaN Photocatalyst Using H_2O as an Electron Donor

Rengui Li,[▽] Wen-Hui Cheng,[▽] Matthias H. Richter, Joseph S. DuChene, Wenming Tian, Can Li, and Harry A. Atwater*

Cite This: *ACS Energy Lett.* 2021, 6, 1849−1856

Read Online

ACCESS | Metrics & More | Article Recommendations | Supporting Information

ABSTRACT: Surface plasmon resonances in metal nanostructures enable the generation of nonequilibrium hot electron−hole pairs, which has received wide interest as a means to drive chemical reactions at the nanoscale. However, harvesting hot holes in plasmonic heterostructures to drive oxidation reactions to balance the photocatalytic CO_2 reduction reaction has been challenging. Further, details of the balanced redox reaction pathways for gas-phase photocatalysis have been difficult to identify. Here, we report an Au/p-GaN plasmonic heterostructure photocatalyst in which unassisted, self-sustaining, highly selective photocatalytic CO_2 reduction to CO is directly balanced by water oxidation, operating under solar illumination. We find remarkable enhancements in CO yield for heterostructures that employ a metal/insulator/semiconductor configuration with an ultrathin aluminum oxide layer between composite Au/Cu nanoparticles and p-GaN. Our work underscores the potential for plasmonic heterostructure photocatalysts to perform selective and unassisted gas-phase photocatalytic CO_2 reduction to convert solar energy into chemical fuels.

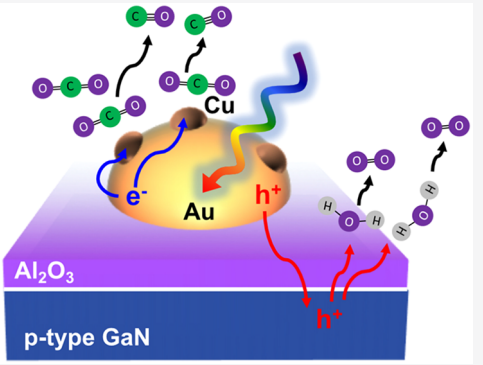

Surface plasmon resonances (SPR) in metal nanostructures enable the generation of nonequilibrium hot electron−hole pairs via plasmon decay, which have received growing research interest as a means to initiate and control chemical reactions at the nanoscale.[1−5] Metal−semiconductor heterostructures are especially promising for plasmon-driven photochemistry thanks to the extended lifetime of the charge-separated state.[6,7] To date, numerous optoelectronic systems have been devised to harness plasmonic hot electrons using noble metal gold (Au) nanoparticles coupled to an n-type semiconductor such as titanium dioxide (TiO_2) for plasmon-driven photocatalysis, including photocatalytic hydrogen production, water oxidation, overall water splitting, and the activation of small molecules.[8−13] Photocatalytic antenna−reactor heterostructures have also been used to drive photodissociation of small molecules along with the reverse water−gas shift reaction.[2,14] However, little attention has been paid to the transfer of plasmonic hot holes from the metal nanoparticles using wide bandgap p-type semiconductors.[1,15] It has been theoretically predicted that for d-band metals like Au, photoexcitation above the interband threshold preferentially generates a favorable distribution of high-energy hot holes with a peak in probability close to that of the incident photon energy.[16,17] Although promising for applications in plasmonic energy conversion devices, capturing these high-energy hot holes for photocatalytic reactions presents considerable challenges. While recent experimental results present related lower energy distributions, only the hot carriers under steady-state conditions were captured instead of the higher-energy nonequilibrium energy distribution, which requires ballistic collection.[18−20] Indeed, the capture of plasmonic hot holes presents a greater challenge than hot electron capture because the mean-free paths of hot holes are even shorter than for hot electrons, typically ∼5−10 nm for hot holes 0−2 eV below the Fermi level compared with ∼20 nm for hot electrons that reside 0−2 eV above the Fermi level.[21−23] Moreover, fewer p-type semiconductors with wide bandgaps are available to provide a feasible path for capturing hot holes from plasmonic metals than n-type semiconductors suited to accepting hot electrons. Thus, harvesting hot holes in

Received: February 21, 2021
Accepted: April 15, 2021
Published: April 20, 2021

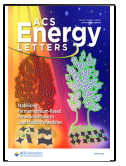

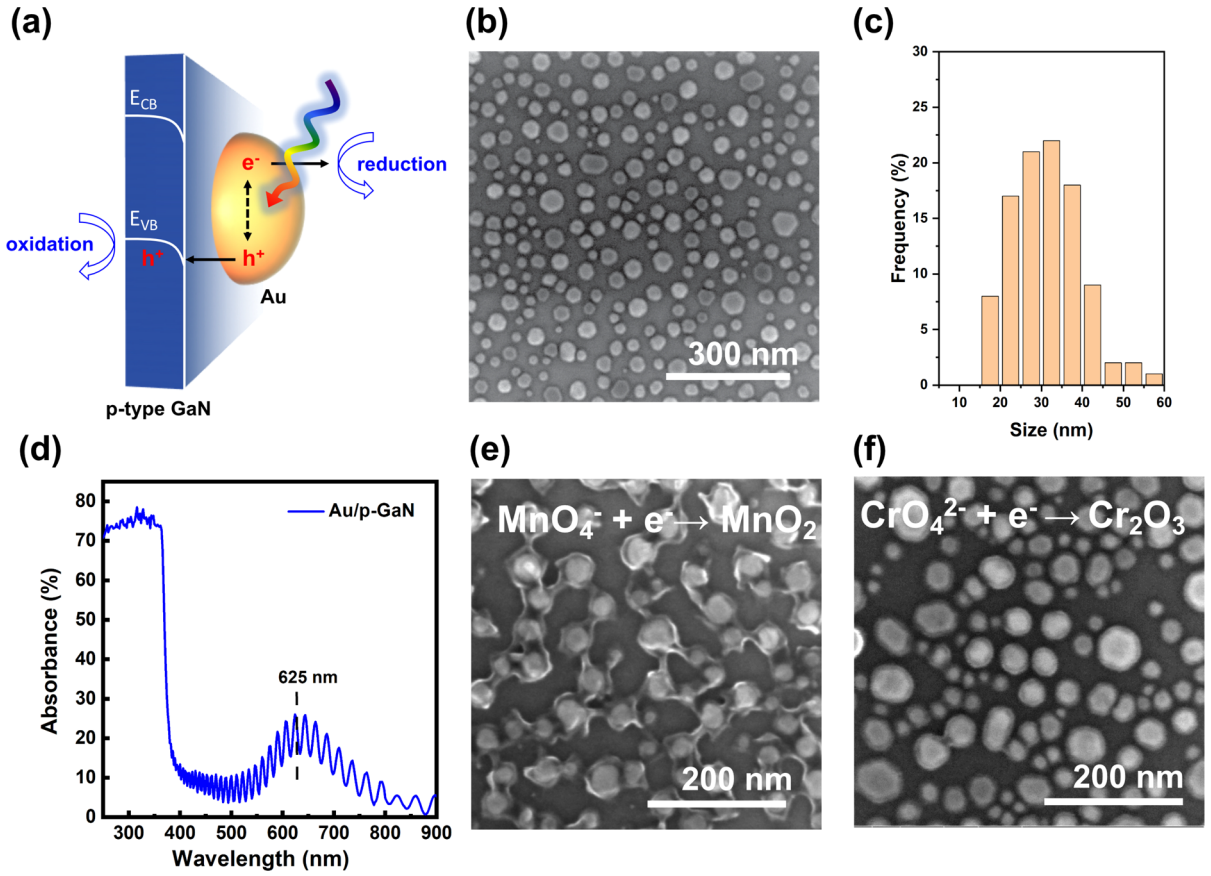

Figure 1. Characterization of plasmonic Au/p-GaN heterostructures for photocatalysis. (a) Illustration of the plasmonic Au/p-GaN heterostructures used for photocatalytic reaction. (b) Scanning electron microscopy (SEM) image of the Au/p-GaN sample. (c) Corresponding Au nanoparticle size distribution. (d) Absorption spectrum of Au/p-GaN heterostructures showing plasmonic absorption feature at 625 nm. (e) SEM image of MnO_2-coated Au nanoparticles after photodeposition from $KMnO_4$ solution with methanol as sacrificial hole scavenger. (f) SEM image of Cr_2O_3-coated Au nanoparticles after photodeposition from K_2CrO_4 solution with methanol as sacrificial hole scavenger.

plasmonic structures for energy conversion reactions is extremely challenging, particularly for thermodynamically unfavorable and kinetically sluggish reactions, like light-induced CO_2 reduction by artificial photosynthesis.[24,25]

While many studies have focused on the capture of hot electrons with metal/semiconductor heterostructures like Au/TiO_2, reports on the capture of plasmonic hot holes by p-type semiconductors are much less common. Previously, we have demonstrated the ability for p-type gallium nitride (p-GaN) to enable hot hole collection from Au nanoparticles (NPs) via formation of an interfacial Schottky barrier (Φ_B > 1.0 eV) and further used these Au/p-GaN photocathodes for photoelectrochemical CO_2 reduction under an applied bias, demonstrating the utility of plasmonic photocathodes for artificial photosynthesis.[1] Very recently, using plasmonic copper (Cu) nanoparticles fabricated onto p-type nickel oxide (p-NiO) photocathodes, we found that optical excitation of plasmonic Cu/p-NiO photocathodes imparts increased selectivity for photoelectrochemical CO_2 reduction to carbon monoxide and formate relative to hydrogen evolution.[15] Nevertheless, these plasmonic photocathodes were realized in aqueous electrolytes in a three-electrode configuration under an applied bias (∼ −1.0 V vs RHE), which provides the additional driving force for charge carrier separation. It would therefore be highly beneficial to alleviate the requirement for an external bias and instead create a self-sustaining plasmonic photocatalyst capable of selective CO_2 conversion that operates without any additional energy inputs. Specifically for photocatalytic CO_2 reduction to chemicals, Ru nanoparticles yielding CH_4;[26] Ag nanoparticles yielding CO, H_2, and formate;[27] and Au nanoparticles yielding CH_4 and C_2H_6 as products have been realized.[28] However, in these previous reports either sacrificial donors were employed or the charge balance and corresponding oxidation reaction needed to balance CO_2 reduction were not determined. To date, there has been no report of plasmonic heterostructures to capture hot holes in photocatalytic CO_2 reduction at zero bias, nor has H_2O been shown to serve as electron donor without any sacrificial reagents.

Here, we demonstrate the first example of gas-phase photocatalytic CO_2 reduction to CO on plasmonic-metal/p-type semiconductor heterostructures without applied bias or the presence of a sacrificial electron donor. We also find that an interfacial layer of aluminum oxide (Al_2O_3) deposited between the plasmonic metal and the underlying p-type semiconductor can significantly improve the interfacial separation of hot holes across the Au/p-GaN heterojunction and that by further decorating Cu nanoparticles onto the Au surface we could accelerate the rate of CO_2 reduction. Overall, our plasmonic Au/p-GaN and Au−Cu/Al_2O_3/p-GaN heterostructures are capable of performing selective, unassisted, gas-phase photocatalytic CO_2 reduction to produce CO balanced by water

https://doi.org/10.1021/acsenergylett.1c00392
ACS Energy Lett. 2021, 6, 1849−1856

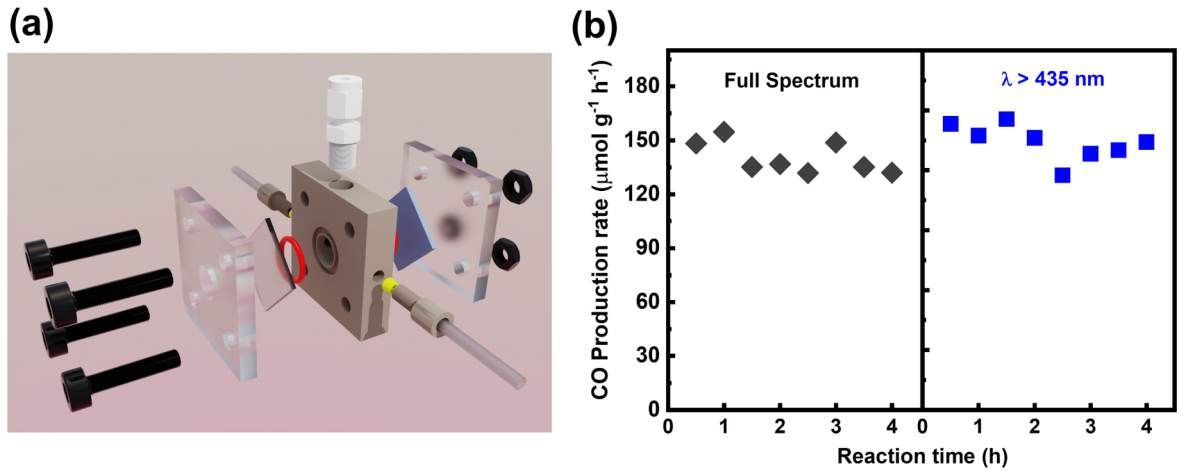

Figure 2. Photocatalytic CO_2 reduction with plasmonic Au/p-GaN heterostructures. (a) Cell configuration for gas-phase CO_2 reduction. (b) CO production rate over time from the Au/p-GaN samples under full spectrum AM 1.5 illumination (black points) and with visible illumination using a 435 nm long pass filter (blue points).

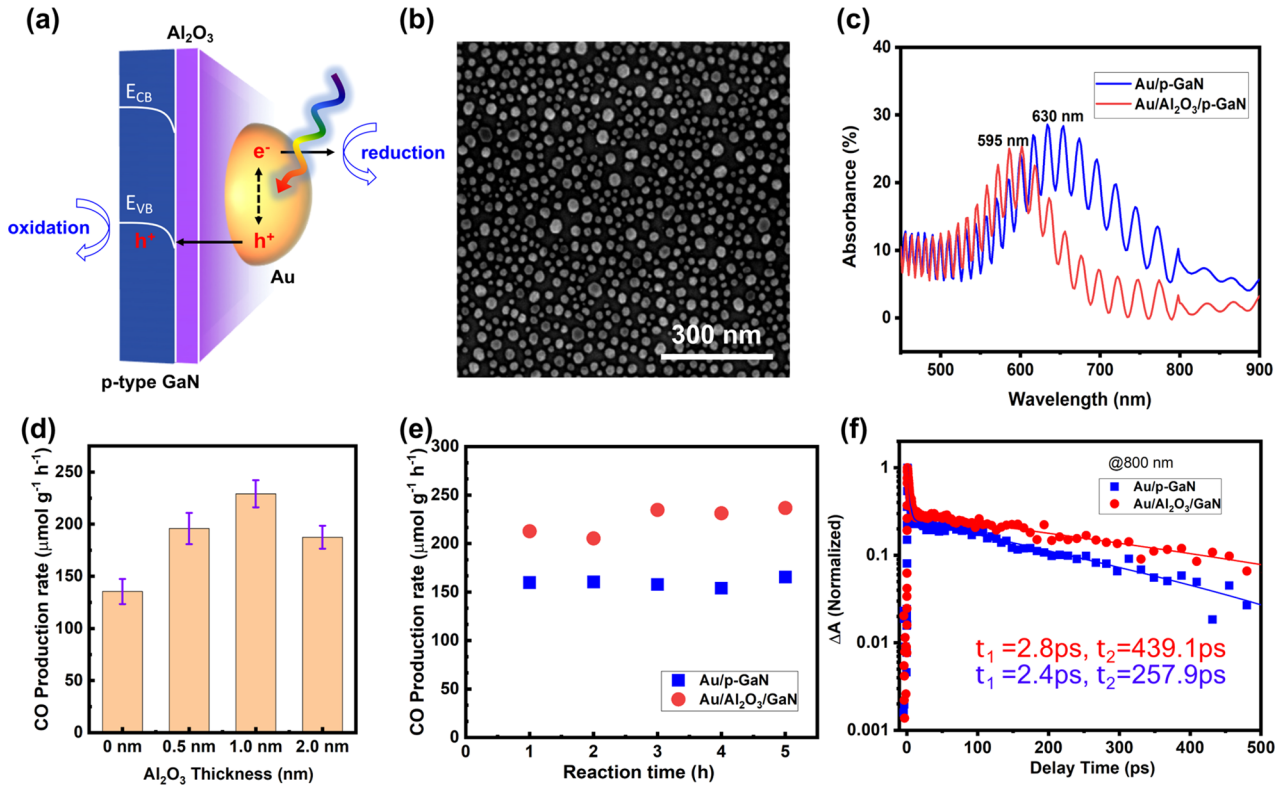

Figure 3. Influence of the Al_2O_3 interfacial layer on the photocatalytic performance of Au/p-GaN and Au/Al_2O_3/p-GaN heterostructures. (a) Illustration of the material configuration of Au/Al_2O_3/p-GaN heterostructures used for photocatalysis. (b) Scanning electron microscopy image of the Au/Al_2O_3/p-GaN samples with an Al_2O_3 layer thickness of 1 nm. (c) Absorption spectra comparison between Au/p-GaN and Au/Al_2O_3/p-GaN samples, showing the plasmonic absorption located at 625 and 595 nm, respectively. (d) Comparison of photocatalytic CO production rate with varying thicknesses of the Al_2O_3 interfacial layer. (e) Photocatalytic CO production over time from the Au/p-GaN and Au/Al_2O_3/p-GaN samples under visible-light illumination (435 nm long pass filter). (f) Transient absorption spectra of the Au/p-GaN and Au/Al_2O_3/p-GaN samples with an excitation wavelength of 600 nm and a probe wavelength of 800 nm. The fitted lifetimes are depicted in the graph.

oxidation to yield O_2. We identify the plasmonic metal (Au or Au−Cu) as the locus of CO_2 reduction and the underlying p-GaN as the locus of water oxidation. Our photocatalytic studies revealed that CO is the only detectable product with negligible contributions from H_2 evolution, implying high reaction selectivity.

Figure 1a shows the working principle of a plasmonic Au/p-GaN heterostructure for gas-phase photocatalytic reaction. The plasmonic Au NPs first absorb light upon illumination, and hot carriers are generated. At the Schottky junction formed between Au and p-GaN, only hot holes with sufficient energy can overcome the barrier, which also limits recombination by preventing the flow of holes back to the metal. Once the holes

https://doi.org/10.1021/acsenergylett.1c00392
ACS Energy Lett. 2021, 6, 1849−1856

are extracted to the p-GaN they are available for oxidation, and the electrons localized in Au NPs can then perform the reduction reaction. We fabricated the Au/p-GaN samples by electron beam evaporation of thin films, and via this process Au NPs were formed after an annealing procedure, as shown in Figure 1b. The diameter of the Au NPs is ∼20−40 nm, and they are relative uniformly distributed on the p-GaN surface. Figure S1 presents the general fabrication process, and details can be found in Methods in the Supporting Information. The morphology for Au/p-GaN samples was measured with atomic force microscopy (AFM) as shown in Figure S2, and the measured particle size distribution is shown in Figure 1c. Figure 1d presents the optical response of the Au/p-GaN samples, with the absorption edge around 365 nm assigned to the bandgap of p-GaN at 3.4 eV. The peak at 625 nm clearly indicates the feature from plasmonic absorption of Au NPs. The fringes present in the absorption spectrum are due to the Fabry−Pérot interferences within the p-GaN layer, consistent with our prior observations.[1]

To probe the location of photogenerated hot electrons in the Au/p-GaN heterostructures, we performed plasmon-driven photoreductive deposition of MnO_2 and Cr_2O_3 using MnO_4^- and CrO_4^{2-} as precursors in the presence of an methanol as a sacrificial hole scavenger (see Methods). We emphasize that these experiments are commonly used in photocatalytic studies to demonstrate the site of redox reactions and that only reduction reactions are possible with these precursors.[12,29−33] As shown in Figure 1e,f, both photo-reduction deposition reactions using photoexcited electrons occur exclusively on the Au NPs while leaving the surface of p-GaN free of any MnO_2 or Cr_2O_3. It is also noted that no MnO_2 or Cr_2O_3 species were observed on either Au or p-GaN substrates under dark conditions, which rules out the possibility of preferential adsorption of MnO_4^- and CrO_4^{2-} ions on the Au/p-GaN surface being responsible for the deposition (Figures S3−S5). Taken together, these results demonstrate that hot electrons preferentially accumulate on the Au NPs under illumination as shown in Figure 1a and that these hot electrons possess enough energy to reduce both MnO_4^- and CrO_4^{2-} precursors under steady-state conditions.

Plasmon-driven photocatalytic CO_2 reduction was conducted within a gas-phase reactor depicted in Figure 2a (see Methods for experimental details). Under full-spectrum AM 1.5 illumination in the presence of both CO_2 and H_2O vapor, we found that the Au/p-GaN heterostructures are capable of reducing CO_2 to CO in the absence of any sacrificial reagents without any detectable H_2 production (Figure 2b, black points). The detailed mass balance of the reaction is included in the Supporting Information. A 435 nm long pass filter was then incorporated to exclude direct interband optical absorption within the p-GaN support (Figure 2b, blue points). A comparable degree of photocatalytic activity was observed for both full spectrum and UV-removed spectral illumination, which reveals that the plasmonic Au NPs are primarily responsible for photocatalytic CO_2 reduction to CO. Therefore, all subsequent photocatalytic experiments employed the long pass filter to exclude any contribution from the p-GaN substrate and focus solely on the plasmonic photocatalytic effect of the metal nanoparticles.

Although the CO_2 reduction can be achieved in Au/p-GaN heterostructures, the activity is still relatively low, possibly because of surface defects that can act as charge-trapping and/or carrier-recombination centers on GaN surfaces. Because oxides are commonly applied to passivate semiconductor surfaces,[34,35] we used a surface engineering approach via atomic layer deposition (ALD) to passivate the surface of our heterostructures. We introduced ALD-deposited Al_2O_3 interfacial layers with different thicknesses and evaluated their influence on photocatalytic CO_2 reduction activity (see Methods). Figure 3a illustrates the device schematic, and Figure 3b presents the scanning electron microscopy (SEM) image of Au/Al_2O_3/p-GaN samples with an Al_2O_3 thickness of ∼1.0 nm; other samples with various Al_2O_3 thicknesses and their associated Au nanoparticle size distributions are shown in Figure S6. We observed a smaller median particle size of 27.5 nm for samples with Al_2O_3 interfacial layers compared with the particle size of 32.5 nm for samples without the interfacial Al_2O_3 layer. Optical measurements revealed a plasmonic absorption peak wavelength of 595 nm for the Au/Al_2O_3/p-GaN as compared with ∼625 nm for Au/p-GaN, as depicted in Figure 3c. While the smaller particle size may partially account for a small blue shift in peak position between samples, the differing dielectric environments is likely more important, where the increased refractive index asymmetry at the Au/Al_2O_3/p-GaN interface is expected to shift the plasmonic resonance to a shorter wavelength relative to Au/p-GaN.

We then conducted gas-phase photocatalytic CO_2 reduction reactions for the Au/Al_2O_3/p-GaN heterostructures as a function of Al_2O_3 thickness as shown in Figure 3d. An optimal activity was found for 1 nm thick Al_2O_3 layers, with a 69% enhancement of the CO production rate as compared to the bare Au/p-GaN sample. Figure 3e shows the CO production rate under visible-light illumination with a 435 nm long pass filter for both samples over a 5 h period. A longer stability test of 30 h duration was also performed for the Au/Al_2O_3/p-GaN samples, shown in Figure S7, indicating photocatalyst durability. We speculate that the reason for the 30% decrement of CO production rate over prolonged operation may be due to moisture condensing on the sample surface that increases Au NP mobility and induces aggregation, because increased Au NP sizes were visualized via SEM at some portions of the substrate after the 30 h reaction (Figure S7). Because slightly different particle size distributions were observed for different Al_2O_3 thicknesses, we calculated the surface area enhancement based on the Au particle size histograms; we found a 7%, 6%, and 14% increase for an Al_2O_3 thickness of 0.5, 1, and 2 nm, respectively, compared to the Au/p-GaN sample. Because the surface area enhancement (∼10%) is still relatively small compared to the 69% enhancement of the CO production rate for the optimal Al_2O_3 layer, we can exclude any difference in surface area as the source of the enhancement in activity. We further conducted transient absorption spectroscopy measurements to examine the effect of the Al_2O_3 interfacial layer on the hot-carrier dynamics, as shown in Figure 3f. An excitation pump pulse wavelength close to the plasmonic resonance at 600 nm and a probe wavelength of 800 nm which is away from the plasmon resonance are chosen. Two decay lifetimes can be seen with multiexponential fitting of the decay process. The faster lifetime (τ_1) can be correlated with carrier−phonon interaction, while we suggest that the slower lifetime (τ_2) corresponds to trap states in GaN.[36,37] The longer lifetime τ_2 (439.1 ps for Au/Al_2O_3/p-GaN and 257.9 ps for Au/p-GaN) observed in samples incorporating Al_2O_3 interfacial layers supports a mechanism in which a reduction of carrier recombination is achieved by surface-defect passivation via

https://doi.org/10.1021/acsenergylett.1c00392
ACS Energy Lett. 2021, 6, 1849−1856

the application of an Al_2O_3 film between the Au NPs and the p-GaN support.

A widely employed approach in photocatalysis involves surface modification with a cocatalyst to improve reaction kinetics. To that end, we further deposited copper (Cu) nanoparticles onto the Au/Al_2O_3/p-GaN heterostructures via electron beam evaporation (see Methods). We note that this approach deposits Cu nanoparticles on both the Au nanoparticles and the underlying substrate without any preference. Direct visualization of the Cu nanoparticles with SEM was challenging because of their very small size of around 5 nm. But it was possible to observe distinctive features in the image that are attributable to the Cu nanoparticles (Figure 4a). The

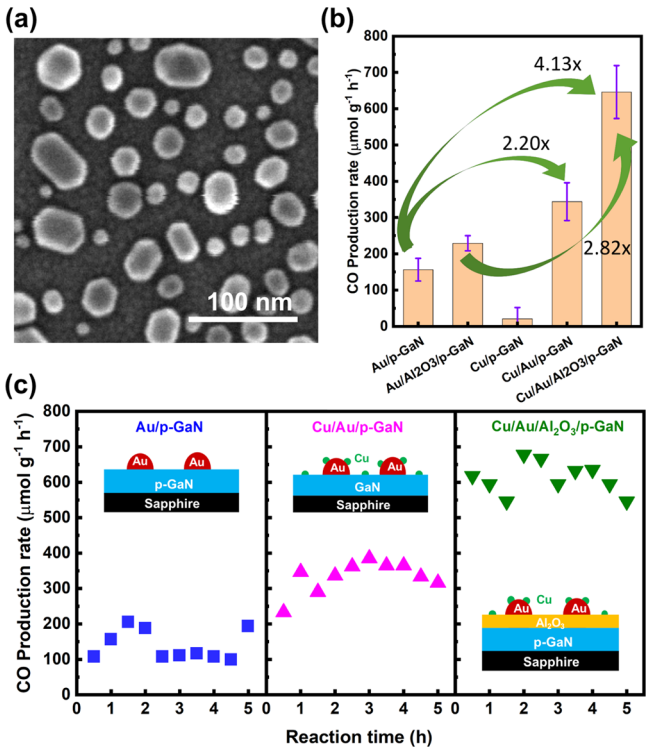

Figure 4. Influence of Cu cocatalysts on photocatalytic activity. (a) Scanning electron microscopy image of the Cu/Au/Al_2O_3/p-GaN heterostructures. (b) Photocatalytic CO production rate comparison of different samples including Au/p-GaN, Au/Al_2O_3/p-GaN, Cu/p-GaN, Cu/Au/p-GaN, and Cu/Au/Al_2O_3/p-GaN under visible-light illumination (435 nm long pass filter). (c) Photocatalytic CO production over time of the Au/p-GaN, Cu/Au/p-GaN, and Cu/Au/Al_2O_3/p-GaN samples under visible-light illumination.

chemical composition of the Cu NPs was examined by X-ray photoelectron spectroscopy as shown in Figure S8. Copper was observed in both metallic (Cu^0) and oxidized forms (Cu^{1+} and Cu^{2+}) on the surface. The benefits of Cu incorporation to overall photocatalytic activity is evident by comparing the CO production rates in Figure 4b: a 120% enhancement of activity was seen relative to the Au/p-GaN sample, and a 182% activity enhancement was found relative to the Au/Al_2O_3/p-GaN sample. The combined use of an interfacial Al_2O_3 layer and the Cu cocatalysts leads to an overall activity enhancement of 313%. Interestingly, Cu/p-GaN heterostructures barely yield any products, indicating that Au NPs are primarily responsible for the plasmonic photocatalysis. The CO production rates from the Au/p-GaN, Cu/Au/p-GaN, and Cu/Au/Al_2O_3/p-GaN samples over a 5 h period are shown in Figure 4c. Overall, these results emphasize the benefits of using Cu cocatalysts and interfacial Al_2O_3 layers for accelerating catalytic reactions and improving interfacial charge separation during plasmon-driven photocatalytic CO_2 reduction.

To confirm that gaseous CO_2 serves as the sole source of CO and that water indeed acts as the electron donor, we performed isotopic labeling experiments using ^{13}CO and $^{18}O_2$ gases as reagents. We conducted independent isotope measurements for both photocatalytic CO_2 reduction and oxygen evolution reaction using gas chromatography−mass spectrometry with the Cu/Au/Al_2O_3/p-GaN heterostructures. Details can be found in Methods in the Supporting Information. Figure S9a shows clear evidence of labeled ^{13}CO production with m/z ratio of 29 upon 2 h of photocatalytic reaction. In addition, Figure S9b confirms labeled $^{18}O_2$ production with m/z ratio of 36 after 12 h of operation.

We performed several additional experiments to elucidate the role of Cu cocatalysts on the observed photocatalytic enhancements. We first synthesized Au/Au/Al_2O_3/p-GaN heterostructures using the same procedure as the Cu/Au/Al_2O_3/p-GaN to duplicate the distinct morphology and associated increase in surface area produced by a two-step deposition process. Photocatalytic studies were then performed to investigate any resulting changes in activity accompanied by such an approach. As shown in Figure S10, the Au/Au/Al_2O_3/p-GaN heterostructures did exhibit enhancements in activity of 37%, but this is far short of the 182% enhancement observed with Cu/Au/Al_2O_3/p-GaN heterostructures. We therefore conclude that the Cu cocatalysts must play another vital role for improving the photocatalytic performance by 182%. The inability to directly measure potential and current in the gas-phase reactor chamber makes it challenging to study the electronic transport pathway. Thus, we prepared samples for photoelectrochemical measurements in a bulk liquid electrolyte. Though a liquid electrolyte cell does not represent the specific operational condition of the gas-phase reactor, photoelectrochemical measurements in the liquid phase with an applied bias provide additional insights about carrier photogeneration and transport in the plasmonic-metal/p-type semiconductor heterostructures. An illustration of the three-electrode setup used for photoelectrohemical measurements is depicted in Figure 5a. Figure 5b shows the current response of the Au/p-GaN (blue), Au/Al_2O_3/p-GaN (red), and Cu/Au/Al_2O_3/p-GaN (green) samples under pulsed illumination with a chopping frequency of 0.05 Hz at a constant applied potential of +0.3 V vs RHE. We observed a slow response time for the Au/p-GaN sample upon on/off illumination. This slow response suggests that photogenerated electrons may gradually accumulate in the Au NPs after hot-hole injection, giving rise to a gradually increasing photocurrent over time. The addition of an Al_2O_3 interfacial layer results in a sharper initial rise and drop of current under chopped illumination, followed by a gradually increasing photocurrent density. Interestingly, a completely different chronoamperometric behavior with faster on/off transitions was seen for Cu/Au/Al_2O_3/p-GaN sample. This suggests that the Cu NPs can more efficiently utilize the hot electrons for the photocatalytic reaction because of the preferable surface chemistry for CO_2 reduction.

We summarize the overall mechanism for plasmon-driven photocatalytic CO_2 reduction in Figure 6. For Au/p-GaN

https://doi.org/10.1021/acsenergylett.1c00392
ACS Energy Lett. 2021, 6, 1849−1856

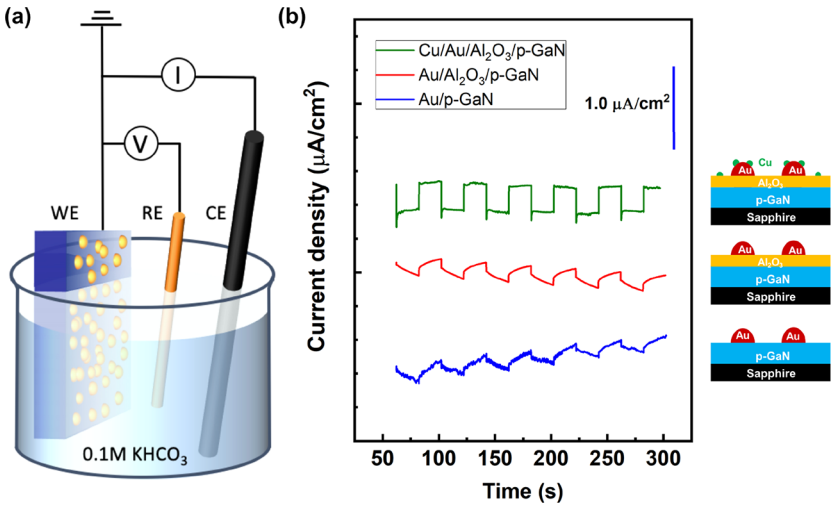

Figure 5. Photoelectrochemical studies of charge separation across the metal/p-type semiconductor interface. (a) Illustration of three-electrode setup with Ag/AgCl reference electrode and carbon rod as counter electrode in 0.1 M $KHCO_3$ electrolyte with various working photocathodes. (b) Chronoamperometry of the Au/p-GaN (blue), Au/Al_2O_3/p-GaN (red), and Cu/Au/Al_2O_3/p-GaN (green) photocathodes under periodic (0.05 Hz) halogen lamp illumination with a 435 nm long pass filter at an applied potential of +0.3 V vs RHE.

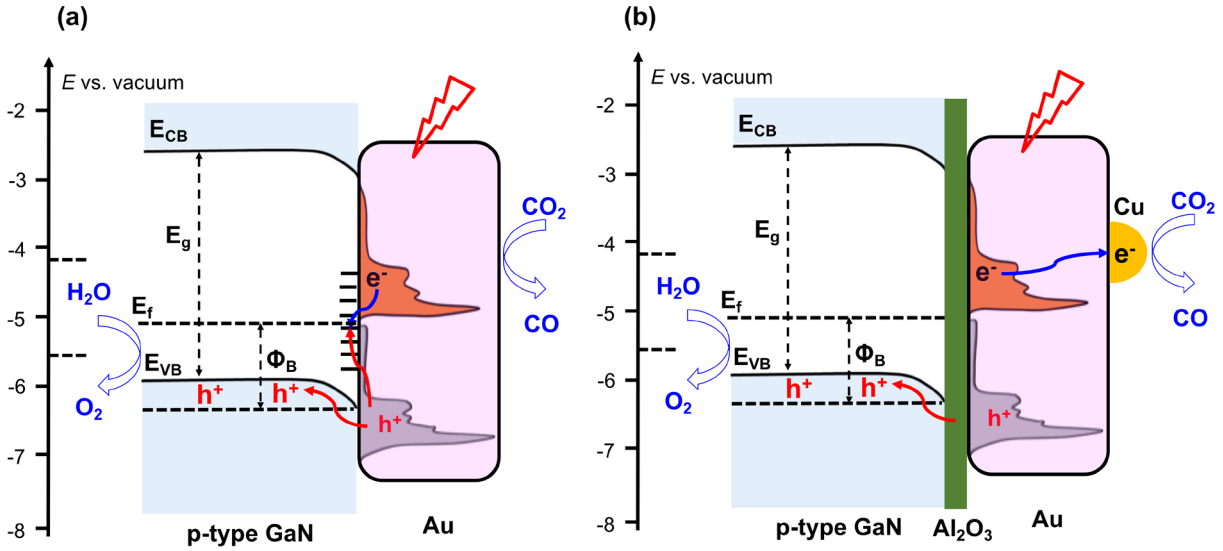

Figure 6. Illustration of the band structure and photocatalytic mechanism of CO_2 reduction balanced by water oxidation. (a) Au/p-GaN heterostructures and (b) Cu/Au/Al_2O_3/p-GaN heterostructures.

(Figure 6a), plasmonic excitation occurs in the Au NPs upon illumination, creating hot electron and hot hole distributions above and below the Au Fermi level (E_F = −5.1 eV vs vacuum). Hot holes with sufficient energy to overcome the barrier height (Φ_B) of 1.1 eV at the Au/p-GaN heterojunction are injected into the p-GaN valence band. However, surface defects on p-GaN can trap some of these charge carriers, enhancing recombination and limiting photocatalytic activity. Hot holes in the p-GaN valence band with energies lower than the oxygen evolution reaction (5.6 eV vs vacuum, considering CO_2 saturated water at pH 3.9) can facilitate water oxidation and molecular oxygen generation. Simultaneously, hot electrons localized in the Au NPs with sufficient energy can drive CO_2 reduction to yield CO (4.26 eV vs vacuum, considering CO_2 saturated water at pH 3.9). The Cu/Au/Al_2O_3/p-GaN heterostructure, with a combination of an Al_2O_3 interfacial layer and Cu cocatalysts, is depicted in Figure 6b. From the transient absorption measurements, we suggest that the Al_2O_3 may passivate surface trap states and reduce carrier recombination. More hot carriers can then be extracted for both oxidation and reduction reactions. Furthermore, increased charge-transfer efficiency to the Cu cocatalysts helps to improve the overall reaction rate.

In conclusion, we have demonstrated a first prototype gas-phase photocatalytic reactor for highly selective, self-sustained, unassisted CO_2 reduction on plasmonic Au/p-GaN photocatalysts, balanced by water oxidation on p-GaN using H_2O as an electron donor. A thin aluminum oxide interfacial layer introduced between the Au nanoparticles and p-GaN was found to significantly improve interfacial carrier separation by reducing recombination processes between injected hot holes within p-GaN and photogenerated hot electrons on the Au nanoparticles. We also observed that decorating Cu nanoparticles on Au surfaces enables a significant enhancement of CO_2 reduction activity. Thus, rationally designed plasmonic heterostructures composed of a plasmonic light absorber (Au),

https://doi.org/10.1021/acsenergylett.1c00392
ACS Energy Lett. 2021, 6, 1849−1856

a hot-hole extractor (p-GaN), an interfacial passivation layer (Al_2O_3), and efficient cocatalysts (Cu) all together result in the most active motif for photocatalytic CO_2 reduction to CO, balanced by water oxidation to O_2. This demonstration illustrates an approach toward the use of hot-carrier photoexcitation in a self-sustaining system for conversion of solar energy into chemical fuels via artificial photosynthesis.

■ ASSOCIATED CONTENT

Supporting Information

The Supporting Information is available free of charge at https://pubs.acs.org/doi/10.1021/acsenergylett.1c00392.

Experimental details for device fabrication, photocatalytic CO_2 reduction, isotope measurement, photoelectrochemical characterization, photoreduction of MnO_2 and Cr_2O_3, long-term stability, and other supporting figures (PDF)

■ AUTHOR INFORMATION

Corresponding Author

Harry A. Atwater − *Joint Center for Artificial Photosynthesis, California Institute of Technology, Pasadena, California 91125, United States; Department of Applied Physics and Material Science, California Institute of Technology, Pasadena, California 91125, United States;* orcid.org/0000-0001-9435-0201; Email: haa@caltech.edu

Authors

Rengui Li − *Joint Center for Artificial Photosynthesis, California Institute of Technology, Pasadena, California 91125, United States; Department of Applied Physics and Material Science, California Institute of Technology, Pasadena, California 91125, United States; State Key Laboratory of Catalysis, Dalian National Laboratory for Clean Energy, Dalian Institute of Chemical Physics, Chinese Academy of Sciences, Dalian 116023, China;* orcid.org/0000-0002-8099-0934

Wen-Hui Cheng − *Joint Center for Artificial Photosynthesis, California Institute of Technology, Pasadena, California 91125, United States; Department of Applied Physics and Material Science, California Institute of Technology, Pasadena, California 91125, United States;* orcid.org/0000-0003-3233-4606

Matthias H. Richter − *Joint Center for Artificial Photosynthesis, California Institute of Technology, Pasadena, California 91125, United States; Division of Chemistry and Chemical Engineering, California Institute of Technology, Pasadena, California 91125, United States;* orcid.org/0000-0003-0091-2045

Joseph S. DuChene − *Joint Center for Artificial Photosynthesis, California Institute of Technology, Pasadena, California 91125, United States; Department of Applied Physics and Material Science, California Institute of Technology, Pasadena, California 91125, United States; Department of Chemistry, University of Massachusetts Amherst, Amherst, Massachusetts 01003, United States;* orcid.org/0000-0002-7145-323X

Wenming Tian − *State Key Laboratory of Molecular Reaction Dynamics, Dynamic Research Center for Energy and Environmental Materials, Dalian Institute of Chemical Physics, Chinese Academy of Sciences, Dalian 116023, China*

Can Li − *State Key Laboratory of Catalysis, Dalian National Laboratory for Clean Energy, Dalian Institute of Chemical Physics, Chinese Academy of Sciences, Dalian 116023, China;* orcid.org/0000-0002-9301-7850

Complete contact information is available at: https://pubs.acs.org/10.1021/acsenergylett.1c00392

Author Contributions

[▽]R.L. and W.-H.C. contributed equally to this work. R.L., W.-H.C., and H.A.A. developed the ideas. R.L. and W.-H.C. fabricated the samples and performed the measurements, with assistance from M.H.R., J.S.D., and W.T. The manuscript was written by R.L., W.-H.C., J.S.D., and H.A.A., with input from all authors. All authors contributed to the discussion and interpretation of results as well as the presentation and preparation of the manuscript.

Notes

The authors declare no competing financial interest.

■ ACKNOWLEDGMENTS

This work was performed by the Joint Center for Artificial Photosynthesis, a DOE Energy Innovation Hub, and was primarily supported through the Office of Science of the U.S. Department of Energy (DOE) under Award No. DE SC0004993 (sample synthesis, gas-phase photocatalytic measurements, and photoelectrochemical measurements), and by the Liquid Sunlight Alliance under Award No. DE-SC0021266 (sample structural and morphological characterization and data analysis). Research was in part carried out at the Molecular Materials Research Center of the Beckman Institute of the California Institute of Technology.

■ REFERENCES

(1) DuChene, J. S.; Tagliabue, G.; Welch, A. J.; Cheng, W.-H.; Atwater, H. A. Hot Hole Collection and Photoelectrochemical CO_2 Reduction with Plasmonic Au/P-GaN Photocathodes. *Nano Lett.* **2018**, *18* (4), 2545−2550.

(2) Zhou, L.; Swearer, D. F.; Zhang, C.; Robatjazi, H.; Zhao, H.; Henderson, L.; Dong, L.; Christopher, P.; Carter, E. A.; Nordlander, P.; Halas, N. J. Quantifying Hot Carrier and Thermal Contributions in Plasmonic Photocatalysis. *Science* **2018**, *362* (6410), 69−72.

(3) Li, S.; Miao, P.; Zhang, Y.; Wu, J.; Zhang, B.; Du, Y.; Han, X.; Sun, J.; Xu, P. Recent Advances in Plasmonic Nanostructures for Enhanced Photocatalysis and Electrocatalysis. *Adv. Mater.* **2021**, *33* (6), 2000086.

(4) Clavero, C. Plasmon-Induced Hot-Electron Generation at Nanoparticle/Metal-Oxide Interfaces for Photovoltaic and Photocatalytic Devices. *Nat. Photonics* **2014**, *8* (2), 95−103.

(5) Linic, S.; Christopher, P.; Ingram, D. B. Plasmonic-Metal Nanostructures for Efficient Conversion of Solar to Chemical Energy. *Nat. Mater.* **2011**, *10* (12), 911−921.

(6) Cortés, E.; Besteiro, L. V.; Alabastri, A.; Baldi, A.; Tagliabue, G.; Demetriadou, A.; Narang, P. Challenges in Plasmonic Catalysis. *ACS Nano* **2020**, *14* (12), 16202−16219.

(7) Linic, S.; Chavez, S.; Elias, R. Flow and Extraction of Energy and Charge Carriers in Hybrid Plasmonic Nanostructures. *Nat. Mater.* **2021**, 1−9.

(8) Tanaka, A.; Teramura, K.; Hosokawa, S.; Kominami, H.; Tanaka, T. Visible Light-Induced Water Splitting in an Aqueous Suspension of a Plasmonic Au/TiO_2 Photocatalyst with Metal Co-Catalysts. *Chem. Sci.* **2017**, *8* (4), 2574−2580.

(9) Huang, J.; He, S.; Goodsell, J. L.; Mulcahy, J. R.; Guo, W.; Angerhofer, A.; Wei, W. D. Manipulating Atomic Structures at the Au/TiO_2 Interface for O_2 Activation. *J. Am. Chem. Soc.* **2020**, *142* (14), 6456−6460.

(10) Collins, G.; Lonergan, A.; McNulty, D.; Glynn, C.; Buckley, D.; Hu, C.; O'Dwyer, C. Semiconducting Metal Oxide Photonic Crystal Plasmonic Photocatalysts. *Adv. Mater. Interfaces* **2020**, *7* (8), 1901805.
(11) Zhan, C.; Wang, Z.-Y.; Zhang, X.-G.; Chen, X.-J.; Huang, Y.-F.; Hu, S.; Li, J.-F.; Wu, D.-Y.; Moskovits, M.; Tian, Z.-Q. Interfacial Construction of Plasmonic Nanostructures for the Utilization of the Plasmon-Excited Electrons and Holes. *J. Am. Chem. Soc.* **2019**, *141* (20), 8053−8057.
(12) Wang, S.; Gao, Y.; Miao, S.; Liu, T.; Mu, L.; Li, R.; Fan, F.; Li, C. Positioning the Water Oxidation Reaction Sites in Plasmonic Photocatalysts. *J. Am. Chem. Soc.* **2017**, *139* (34), 11771−11778.
(13) Mubeen, S.; Lee, J.; Singh, N.; Krämer, S.; Stucky, G. D.; Moskovits, M. An Autonomous Photosynthetic Device in Which All Charge Carriers Derive From Surface Plasmons. *Nat. Nanotechnol.* **2013**, *8* (4), 247−251.
(14) Robatjazi, H.; Zhao, H.; Swearer, D. F.; Hogan, N. J.; Zhou, L.; Alabastri, A.; McClain, M. J.; Nordlander, P.; Halas, N. J. Plasmon-Induced Selective Carbon Dioxide Conversion on Earth-Abundant Aluminum-Cuprous Oxide Antenna-Reactor Nanoparticles. *Nat. Commun.* **2017**, *8* (1), 27.
(15) DuChene, J. S.; Tagliabue, G.; Welch, A. J.; Li, X.; Cheng, W.-H.; Atwater, H. A. Optical Excitation of a Nanoparticle Cu/P-NiO Photocathode Improves Reaction Selectivity for CO_2 Reduction in Aqueous Electrolytes. *Nano Lett.* **2020**, *20* (4), 2348−2358.
(16) Liu, J. G.; Zhang, H.; Link, S.; Nordlander, P. Relaxation of Plasmon-Induced Hot Carriers. *ACS Photonics* **2018**, *5* (7), 2584−2595.
(17) Tagliabue, G.; Jermyn, A. S.; Sundararaman, R.; Welch, A. J.; DuChene, J. S.; Pala, R.; Davoyan, A. R.; Narang, P.; Atwater, H. A. Quantifying the Role of Surface Plasmon Excitation and Hot Carrier Transport in Plasmonic Devices. *Nat. Commun.* **2018**, *9* (1), 3394.
(18) Kim, Y.; Dumett Torres, D.; Jain, P. K. Activation Energies of Plasmonic Catalysts. *Nano Lett.* **2016**, *16* (5), 3399−3407.
(19) Pensa, E.; Gargiulo, J.; Lauri, A.; Schlucker, S.; Cortes, E.; Maier, S. A. Spectral Screening of the Energy of Hot Holes Over a Particle Plasmon Resonance. *Nano Lett.* **2019**, *19* (3), 1867−1874.
(20) Reddy, H.; Wang, K.; Kudyshev, Z.; Zhu, L.; Yan, S.; Vezzoli, A.; Higgins, S. J.; Gavini, V.; Boltasseva, A.; Reddy, P.; Shalaev, V. M.; Meyhofer, E. Determining Plasmonic Hot-Carrier Energy Distributions via Single-Molecule Transport Measurements. *Science* **2020**, *369* (6502), eabb3457.
(21) Bernardi, M.; Mustafa, J.; Neaton, J. B.; Louie, S. G. Theory and Computation of Hot Carriers Generated by Surface Plasmon Polaritons in Noble Metals. *Nat. Commun.* **2015**, *6* (1), 7044.
(22) Brown, A. M.; Sundararaman, R.; Narang, P.; Goddard, W. A., III; Atwater, H. A. Nonradiative Plasmon Decay and Hot Carrier Dynamics: Effects of Phonons, Surfaces, and Geometry. *ACS Nano* **2016**, *10* (1), 957−966.
(23) Valenti, M.; Venugopal, A.; Tordera, D.; Jonsson, M. P.; Biskos, G.; Schmidt-Ott, A.; Smith, W. A. Hot Carrier Generation and Extraction of Plasmonic Alloy Nanoparticles. *ACS Photonics* **2017**, *4* (5), 1146−1152.
(24) Ross, M. B.; De Luna, P.; Li, Y.; Dinh, C. T.; Kim, D.; Yang, P.; Sargent, E. H. Designing Materials for Electrochemical Carbon Dioxide Recycling. *Nat. Catal.* **2019**, *2* (8), 648−658.
(25) Seh, Z. W.; Kibsgaard, J.; Dickens, C. F.; Chorkendorff, I.; Nørskov, J. K.; Jaramillo, T. F. Combining Theory and Experiment in Electrocatalysis: Insights Into Materials Design. *Science* **2017**, *355* (6321), No. eaad4998.
(26) Zhang, X.; Li, X.; Zhang, Du; Su, N. Q.; Yang, W.; Everitt, H. O.; Liu, J. Product Selectivity in Plasmonic Photocatalysis for Carbon Dioxide Hydrogenation. *Nat. Commun.* **2017**, *8* (1), 14542.
(27) Kumari, G.; Zhang, X.; Devasia, D.; Heo, J.; Jain, P. K. Watching Visible Light-Driven CO_2 Reduction on a Plasmonic Nanoparticle Catalyst. *ACS Nano* **2018**, *12* (8), 8330−8340.
(28) Yu, S.; Wilson, A. J.; Heo, J.; Jain, P. K. Plasmonic Control of Multi-Electron Transfer and C−C Coupling in Visible-Light-Driven CO_2 Reduction on Au Nanoparticles. *Nano Lett.* **2018**, *18* (4), 2189−2194.
(29) Li, R.; Zhang, F.; Wang, D.; Yang, J.; Li, M.; Zhu, J.; Zhou, X.; Han, H.; Li, C. Spatial Separation of Photogenerated Electrons and Holes Among {010} and {110} Crystal Facets of $BiVO_4$. *Nat. Commun.* **2013**, *4* (1), 1432.
(30) Li, D.; Chen, R.; Wang, P.; Li, Z.; Zhu, J.; Fan, F.; Shi, J.; Li, C. Effect of Facet-Selective Assembly of Cocatalyst on $BiVO_4$ Photoanode for Solar Water Oxidation. *ChemCatChem* **2019**, *11* (16), 3763−3769.
(31) Nishimura, N.; Tanikawa, J.; Fujii, M.; Kawahara, T.; Ino, J.; Akita, T.; Fujino, T.; Tada, H. A Green Process for Coupling Manganese Oxides with Titanium(IV) Dioxide. *Chem. Commun.* **2008**, 3564−3566.
(32) Maeda, K.; Teramura, K.; Lu, D.; Saito, N.; Inoue, Y.; Domen, K. Roles of Rh/Cr_2O_3 (Core/Shell) Nanoparticles Photodeposited on Visible-Light-Responsive $(Ga_{1-X}Zn_X)(N_{1-X}O_X)$ Solid Solutions in Photocatalytic Overall Water Splitting. *J. Phys. Chem. C* **2007**, *111* (20), 7554−7560.
(33) Hugonnot, E.; Delville, M.-H.; Delville, J.-P. Universal Behavior of Photochemical Deposition in Liquid Solutions Driven by a One-Photon Transition. *Phys. Rev. E* **2007**, *75* (6), 061602.
(34) Lyons, J. L.; Van de Walle, C. G. Computationally Predicted Energies and Properties of Defects in GaN. *NPJ. Comput. Mater.* **2017**, *3* (1), 12.
(35) Winnerl, A.; Garrido, J. A.; Stutzmann, M. GaN Surface States Investigated by Electrochemical Studies. *Appl. Phys. Lett.* **2017**, *110* (10), 101602.
(36) Tagliabue, G.; DuChene, J. S.; Abdellah, M.; Habib, A.; Gosztola, D. J.; Hattori, Y.; Cheng, W.-H.; Zheng, K.; Canton, S. E.; Sundararaman, R.; Sa, J.; Atwater, H. A. Ultrafast Hot-Hole Injection Modifies Hot-Electron Dynamics in Au/p-GaN Heterostructures. *Nat. Mater.* **2020**, *19*, 1312−1318.
(37) Ye, H.; Wicks, G. W.; Fauchet, P. M. Hot Hole Relaxation Dynamics in p-GaN. *Appl. Phys. Lett.* **2000**, *77* (8), 1185−1187.

https://doi.org/10.1021/acsenergylett.1c00392
ACS Energy Lett. 2021, 6, 1849−1856